11-23-2005

Performance of a C4F8O Gas Radiator Ring Imaging Cherenkov Detector Using Multi-anode Photomultiplier Tubes

Raymond Mountain
Syracuse University

Marina Artuso
Syracuse University

Chaouki Boulahouache
Syracuse University

S. Blusk
Syracuse University

SUHEP-10-2005
May 17, 2005

Performance of a C_4F_8O Gas Radiator Ring Imaging Cherenkov Detector Using Multi-anode Photomultiplier Tubes

M. Artuso, C. Boulahouache, S. Blusk, J. Butt,
O. Dorjkhaidav, N. Menaa, R. Mountain, H. Muramatsu,
R. Nandakumar, K. Randrianarivony, R. Sia, T. Skwarnicki, S. Stone,
J. C. Wang and K. Zhang [1]

Physics Department, 201 Physics Building
Syracuse University, Syracuse, NY 13244-1130

Abstract

We report on tests of a novel ring imaging Cherenkov (RICH) detection system consisting of a 3 meter long gaseous C_4F_8O radiator, a focusing mirror, and a photon detector array based on Hamamatsu multi-anode photomultiplier tubes. This system was developed to identify charged particles in the momentum range from 3-70 GeV/c for the BTeV experiment.

PACS numbers: 03.30+p, 07.85YK

1 INTRODUCTION

Ring imaging Cherenkov (RICH) detection has proven to be a most useful way to distinguish the identities of charged particles, both hadrons and leptons, in high energy physics experiments [1]. We report on measurements of Cherenkov ring images using a 3 meter long octafluorotetrahydrofuran, C_4F_8O, gas radiator and Hamamatsu multi-anode photomultiplier tubes (MAPMT), model R8900-M16, to measure the Cherenkov angle. This gas has never been used before in this application and the tubes are new versions that also have not been tested. This system was designed for the now defunct BTeV experiment

[1] Supported by the National Science Foundation

planned for Fermilab. The main design criteria was the ability to separate charged pions from kaons at the four standard deviation level for momenta between 3 and 70 GeV/c. We intended to achieve this separation by detecting about 40 photons, each with angular resolution of 0.75 mr. We show how we derive these expectations below.

The tests were done using a 120 GeV/c proton beam at Fermilab. We constructed a full length version of the detector that had, however, a smaller width and used a single spherical focusing mirror. The full system is described in Ref. [2].

This system was originally designed using C_4F_{10} as a radiator. The production of this gas, however, has been ended; the last known supplier, the 3M corporation, has informed us that they do not intend further manufacture. Thus although stockpiles of the gas exist, the long term prospects for use in physics detectors are not good. We will show that C_4F_8O provides an excellent alternative.

2 APPARATUS

2.1 Introduction

The basic components of the test system are shown in Fig. 1. The tank contains the gas in both arms. The beam traverses 3 meters of gas in one arm in which it generates Cherenkov light. The light is reflected by a spherical focusing mirror onto an array of MAPMTs. These tubes are placed in their own enclosure so we could work on them without opening the radiator gas volume. They are separated from the gas volume by a 0.64 cm thick UVT acrylic window. The MAPMT readout consists of specialized front end electronics developed in conjunction with IDE-AS of Oslo, Norway. These devices are mounted on hybrids connected a PCI based data acquisition system described below. We now discuss properties of each of these items.

2.2 Mirror and Optics

The mirror was produced by the COMPAS Consortium (Czech Republic). It is made of glass with an aluminized front face having an hexagonal shape 60 cm across each diagonal point-to-point. The radius of curvature was measured to be 659 cm by finding the focal position of the light from a small source reflected off the entire mirror surface. The same technique allowed for measurement

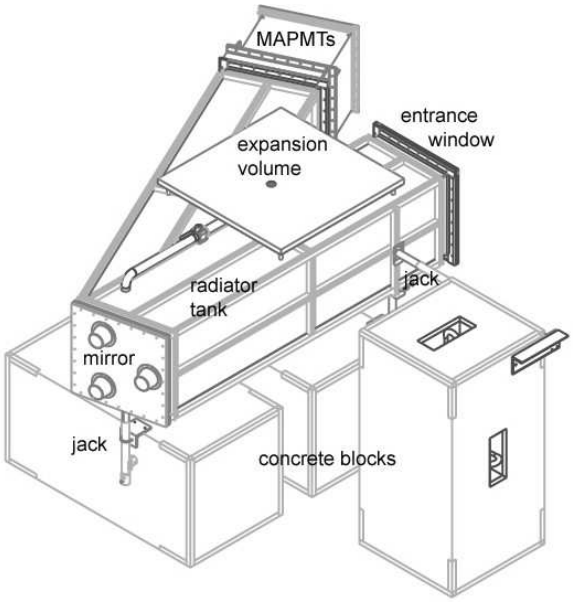

Fig. 1. Schematic of the test apparatus. The beam particles entered at the entrance window and traversed 3 meters of gas. The Cherenkov photons were focussed by mirror onto the MAPMTs.

of the spot size, defined as the diameter of the circle that contains 95% of the reflected light. For this mirror the spot size is 2.97 mm. This is small enough that any dispersive effects due to mirror quality will be negligible. The reflectivity of the mirror versus wavelength is shown in Fig. 2 [3]. Note that the 81% reflectivity around 300 nm is somewhat lower than the 85% specified by COMPAS and significantly lower than the 90% reflectivity measured for the HERA-b mirrors [4], made using a similar technology.

The transparency of a sample of the plastic used for the acrylic window with a different thickness, 0.37 cm, is shown as a function of wavelength in Fig. 3 along with the transparency of a 0.08 cm thick sample of glass used in the MAPMTs. The glass measurements are from Hamamatsu and repeated by us. Our measurements were made using a spectrophotometer system, that is described in detail in Appendix A.2 of ref. [5]. The errors on the measurement are $\pm 1\%$, absolute, at all wavelengths. Our system is designed to work in the wavelength region from approximately 280 nm to about 600 nm, where the quantum efficiency of the MAPMTs falls to zero. The product of the acrylic window and MAPMT window transmission is also shown on Fig. 3, where the transmission for the actual material thickness are used.

2.3 MultiAnode-PhotoMulitplierTubes

Our 53 MAPMTs were arranged in an approximate circle, as shown in Fig. 4, in order to intercept most of the Cherenkov ring. A few were purposely displaced

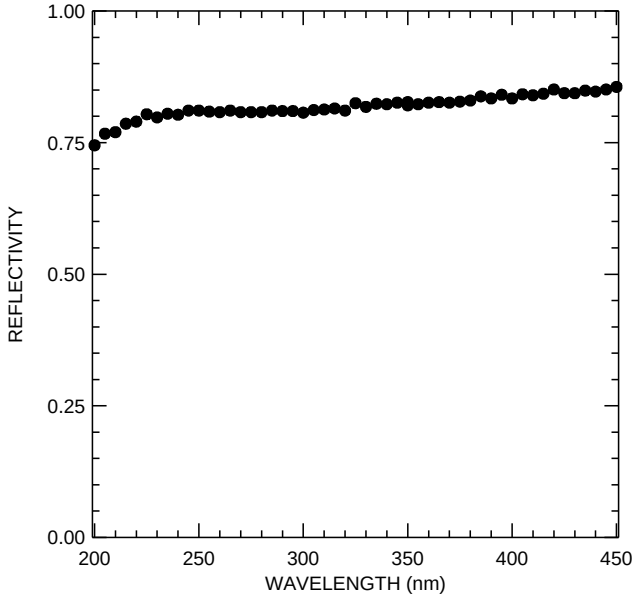

Fig. 2. Measurement of mirror reflectivity, in the center of the mirror, versus wavelength.

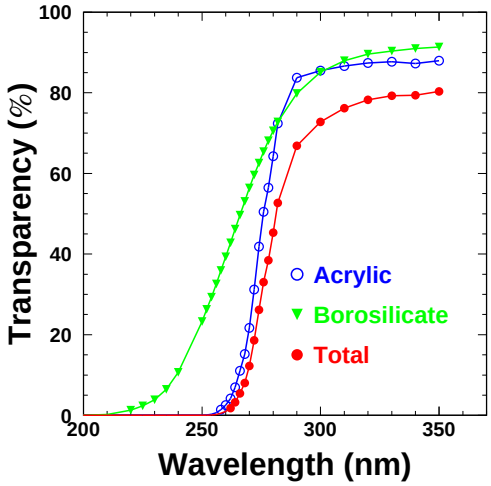

Fig. 3. The transparency as a function of wavelength for 0.08 cm thick Hamamatsu borosilcate glass (inverted triangles), and 0.37 cm thick Polymer Plastics ultraviolet transmitting acrylic plate (open circles). Also shown is the transmission through both for the actual used thicknesses of 0.08 cm of glass and 0.64 cm of acrylic (filled circles).

to be able to monitor noise or backgrounds. The tubes and the electronics were water cooled. The temperature varied from 26°-33°C, depending on the vertical position and was kept constant within ±0.2°C when running at our nominal voltage settings.

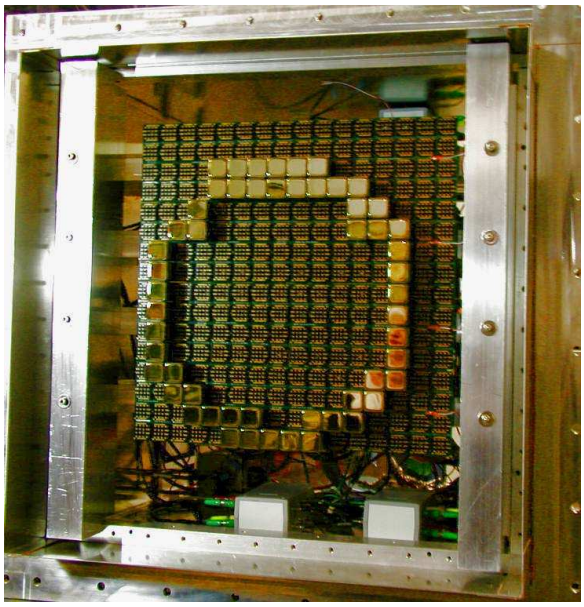

Fig. 4. A photograph of the MAMPT system mounted on the high voltage baseboards.

The R8900-M16 multianode photomultiplier tube (MAPMT) is a 26.2 mm × 26.2 mm square PMT with a 0.8 mm thick borosilicate glass window and a Bialkali (K-Cs) photocathode. The active area of the photocathode is specified to be 24 mm × 24 mm. The tube is segmented into a 4 × 4 array of independent photodetection elements. Each cell has its own 12-stage dynode chain connected to an anode output. A photograph of the MAPMT is shown in Fig. 6. A single HV line and a voltage divider network (VDN) provide voltages to the photocathode and the dynodes. A schematic of the VDN is shown in Fig. 7. In our initial studies of the tubes, and for the results presented in this section we used resistances of 110 kΩ, 330 kΩ, 330 kΩ, and 110kΩ for R1-R4, 180 kΩ for R5-R15, 1 MΩ for R16, 51 Ω for R17-R19, and 20kΩ for R20, as recommended by Hamamatsu. The capacitors, C1-C4 are all 0.01 μF, 200 V. Gains for individual tubes varied in the range 1-4× 10^6 at 800 V. More important for our purposes is the gain variations within a tube, since they can't be reduced by tuning voltage settings. Fig. 5 shows the r.m.s. variations within each of our tubes. The channel-to-channel gain variation within a tube, averaged over all tubes, has an r.m.s. width of 16%.

For the test beam run we decided to run at lower voltages in order to have less gain. In order to maintain full collection efficiency, we use a different set of resistances in the first four stages (R1-R4) of 180 kΩ, 536 kΩ, 536 kΩ, and 180kΩ, the rest staying the same. These voltage dividers were implemented on baseboards that host 16 MAPMT's each. The baseboards also transmit the MAPMT signals via flat multiconductor cables to hybrid boards that host the electronics.

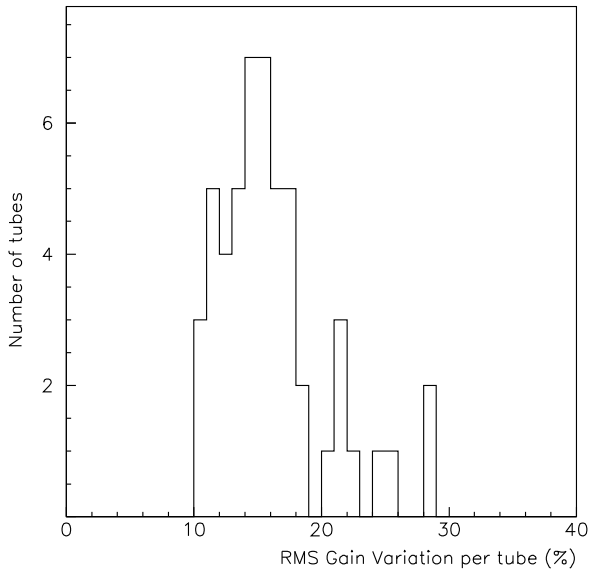

Fig. 5. The r.m.s. gain variations within each tube.

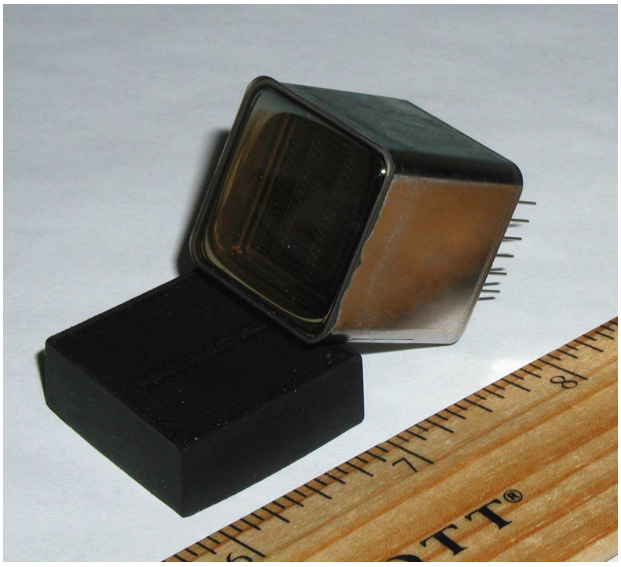

Fig. 6. Photograph of a R8900-M16 MAPMT.

The R8900 is the result of an evolution of MAPMTs from Hamamatsu which began with tubes with active area as low as 36% (R5900) and culminated with this tube which is designed to have an active area approaching 85%.

We performed a series of bench tests including: comparison of the pulse height spectra from channel-to-channel, determination of the active area, and measurement of the sensitivity to external magnetic fields. These tests were performed using a low-intensity blue LED, wavelength of 470 nm with a spread having a full width at half maximum of 40 nm, whose light was transported inside a dark-box along a single-mode optical fiber. The tip of the fiber was pointed at the center of each channel and the pulse height spectra was measured using a PCI-based ADC card. The voltage was set to 850 V for these

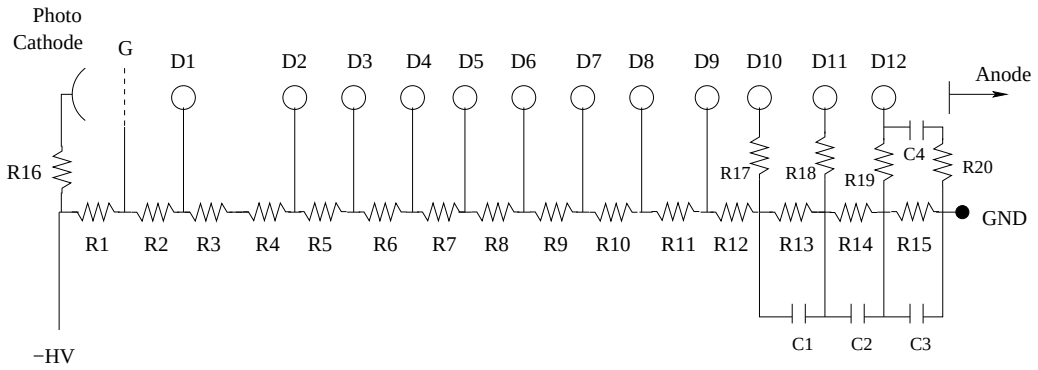

Fig. 7. Electrical schematic of the voltage divider network. Resistors (R) and capacitors (C) are indicated. The D's indicate dynodes, and G is the focusing grid.

initial measurements. The pulse height spectra for one of the MAPMTs are shown in Fig. 8. The channel-to-channel gain variations are at the level of 15-20%. Most of the channels have a well-defined peak and valley, although channels 6, 10, and 12 have a larger fraction of low pulse height signals. This is not a significant problem since the VA_MAPMT chip (see Section 2.5) which is used for the MAPMT readout can operate at low threshold.

To investigate the active area of the tube and the magnetic field sensitivity, the signals from the MAPMT were read out using CAMAC and a LabVIEW-based DAQ. The CAMAC system includes an amplifier (LeCroy #612A), discriminator (Phillips Scientific, #710) and scaler (LeCroy #2551). The threshold was set to a relatively high value, which resulted in some clipping of low pulse height signals, although for these studies, we were mainly interested in relative response.

For the active area determination, we scan over the face of the MAPMT in steps of 0.25 mm in both X and Y. The light from the fiber was passed through an additional collimator which provided, on the face of the tube, an approximately Gaussian shaped spot in both X and Y dimensions with an r.m.s. width of about 150 μm. A sketch of the collimator is shown in Fig. 9. The tubes are positioned 1 mm away from the tip of the fiber with an accuracy of 0.5 mm. The fiber position is determined to 20 μm precision in both X and Y and the rotational accuracy is 20 mr. At each point we measure the total number of counts above the discriminator threshold in a time interval of 2 seconds. The dark count rate was typically about 40 Hz and was therefore neglected. The results of a typical scan are shown in Fig. 10 where we plot the integrated count rate as a function of the (X,Y) coordinates of the spot. The outline of the tube is evident. A 24 mm square box is superimposed, which shows that the active area in X is about 24 mm, while in Y it is closer to 23 mm. The asymmetry of the dynode structure may account for this difference.

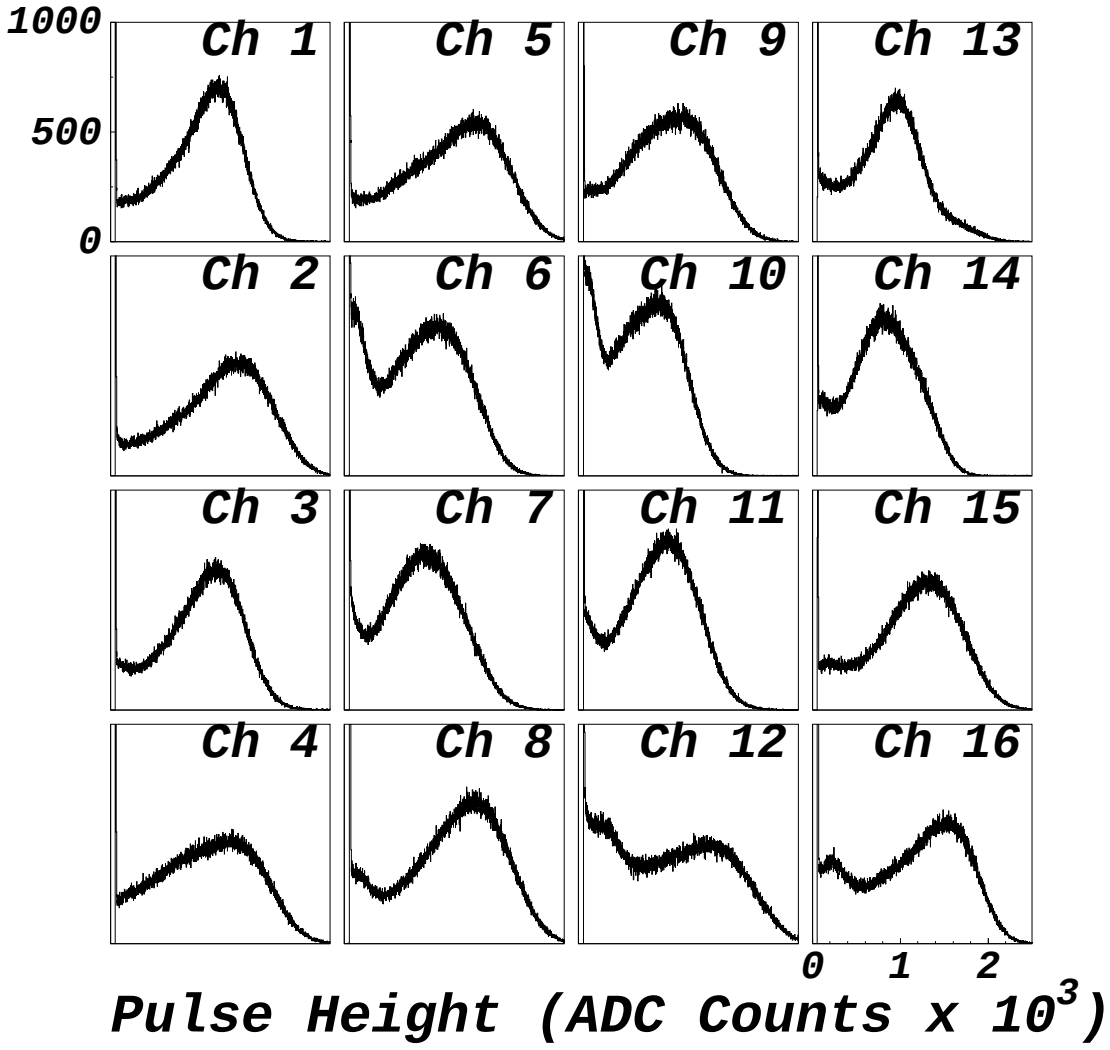

Fig. 8. Pulse height spectra for one of the R8900 MAPMTs, where all of the 16 channels are shown in their proper geometrical positions. (All the horizontal and vertical scales are the same.)

These data indicate that 80% of the tube's physical area is active. Counts outside the box are due to background which has not been subtracted.

The individual channel responses are more clearly illustrated in Fig. 11, where we project out a slice of Fig. 10 along (a) X and (b) Y, such that the slice passes through the center of a row and a column. The unshaded histogram shows the integrated count rate for all channels and the shaded histograms show the contributions from the individual channels in that particular row or column. The sharp drop off at the edge of the photocathode confirms the small spot size. Near the border of neighboring channels, we observe a region of ambiguity where a photon can be focused onto the first dynode of either

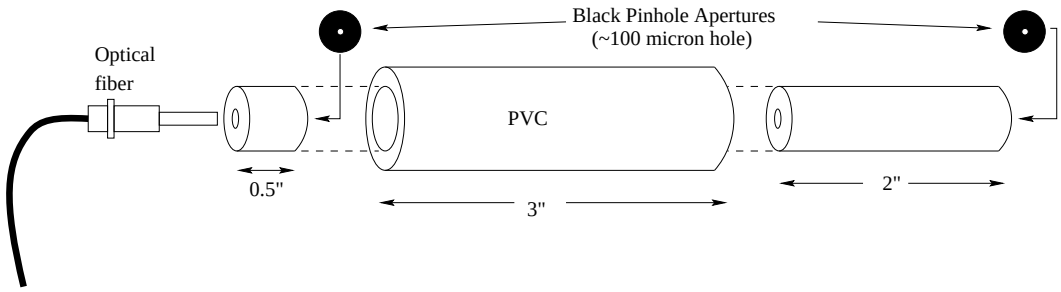

Fig. 9. A sketch of the collimator used for the MAPMT scan.

channel. Once in that channel, it is expected that the signal will be collected on the corresponding anode. To quantify this effect, we fit the edge to an error function and extract an r.m.s. width of 0.75 mm, after a small correction for the size of the light spot (∼0.15 mm). Alternately, we compute the fraction of counts which falls outside the geometric edge of a channel relative to the total counts within the 6 mm x 6 mm boundary. We find that about 5% of the counts spill over into a neighboring channel for each edge. Therefore, for an interior channel, about 20% of the total counts are detected on neighboring channels; this corresponds to 5% for each of the four neighbors. These photons are generally close to the periphery, as indicated by the roll off at the edge of the channels (see Fig. 11). This leads to a small degradation in the positional resolution of this device relative to one which has no spill over.

Lastly, we report on measurements of the magnetic field sensitivity of the R8900-M16 MAPMT. For use in BTeV, we required the tubes to perform well in an external field as large as 10 Gauss. We studied two corner channels (channels 1 and 13), one non-corner edge channel (channel 3) and one interior channel (channel 10). (For some tests we included another corner channel 16.) The tests consisted of measuring the count rate from a pulsed LED with zero field and then with a known field provided by a pair of Helmholtz coils. We investigated both the orientation parallel to the axis of the tube (longitudinal field)and perpendicular (transverse field).

The results of applying a longitudinal magnetic field on the tube without shielding are shown in Fig. 12. The efficiency was mildly dependent upon the transverse field, dropping by ∼10% with a transverse field of 15 Gauss for a corner channel, and by less than 5% for interior channels. On the other hand, significant losses in collection were observed when longitudinal fields were applied.

We investigated shielding the tube with a 1 inch long 250 μm thick mu-metal shield. The shield was electrically isolated from the outer can of the MAPMT and was allowed to float electrically. Count rate measurements were taken with different extension lengths, d, of the mu-metal tube beyond the face of the MAPMT. Data were taken for d=0 mm, 5 mm, and 10 mm. The results are

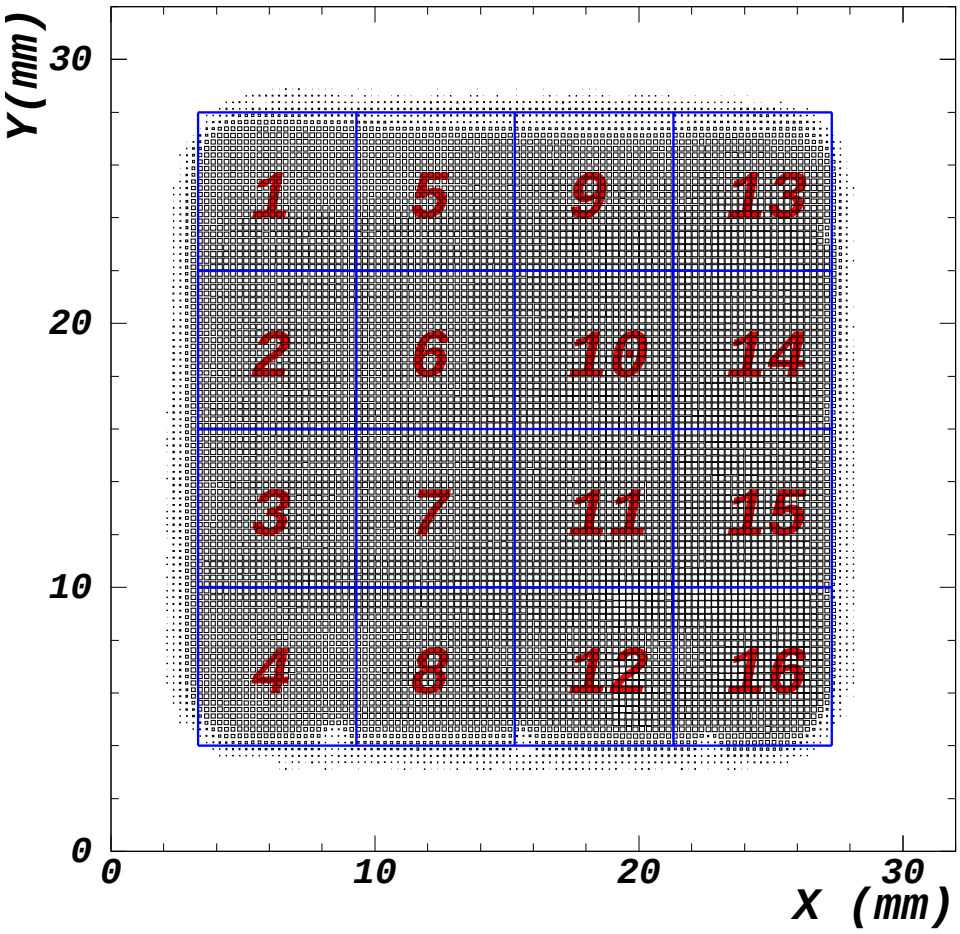

Fig. 10. Two dimensional scan of an R8900-M16 MAPMT. Both the X and Y step sizes are 0.25 mm. The channel geometry is shown in the boxes. The data have not been background subtracted (see text).

shown in Fig. 13 for channels 1, 3, 10, and 16. Each set of data are normalized to the count rate at zero applied field. We find that when the shields are not extended (d=0 mm), the corner and edge channels incur large losses, coming from both collection efficiency and a decrease in gain; in fact, there is almost no shielding effect in this configuration. As the shielding is extended the losses are reduced, and at 10 mm, the drop in efficiency (at 10 Gauss) is typically less than 10%. Some channels show an increase in count rate as compared to no field, and hence the average loss is typically less than 5%.

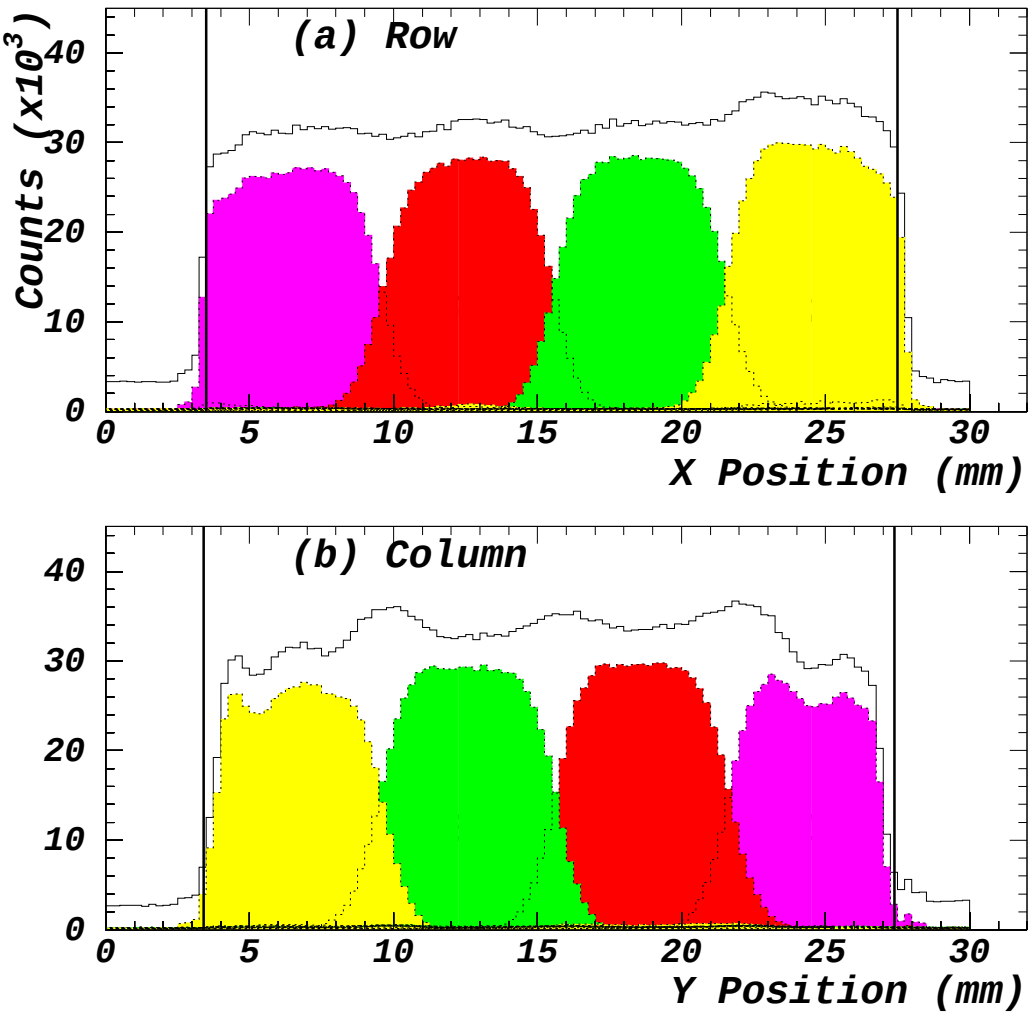

Fig. 11. Slice, 0.25 mm wide, of the two-dimensional XY scan along 4 rows of the R8900 passing through the center of the channels. Step sizes are 0.25 mm in X and Y. The unshaded histogram is the sum of all channels while the shaded histograms correspond to individual channels.

2.4 Beam Properties

The beam test data was taken at Fermi National Accelerator Laboratory, in the Meson Test Beam Facility (MTBF) [6]. The RICH detector was set up in the MT6B enclosure. The beam as delivered was 120 GeV protons, from the resonant extraction of a single Booster batch in the Main Injector, with a <4% momentum bite. The beam tune was varied somewhat during the several days of data-taking, but typical beam rates were 5 KHz per spill, as measured by beam counters. Spills lasted 700 ms, with 1 to 8 spills per supercycle (60 s). The data-taking runs lasted on the order of 30 mins.

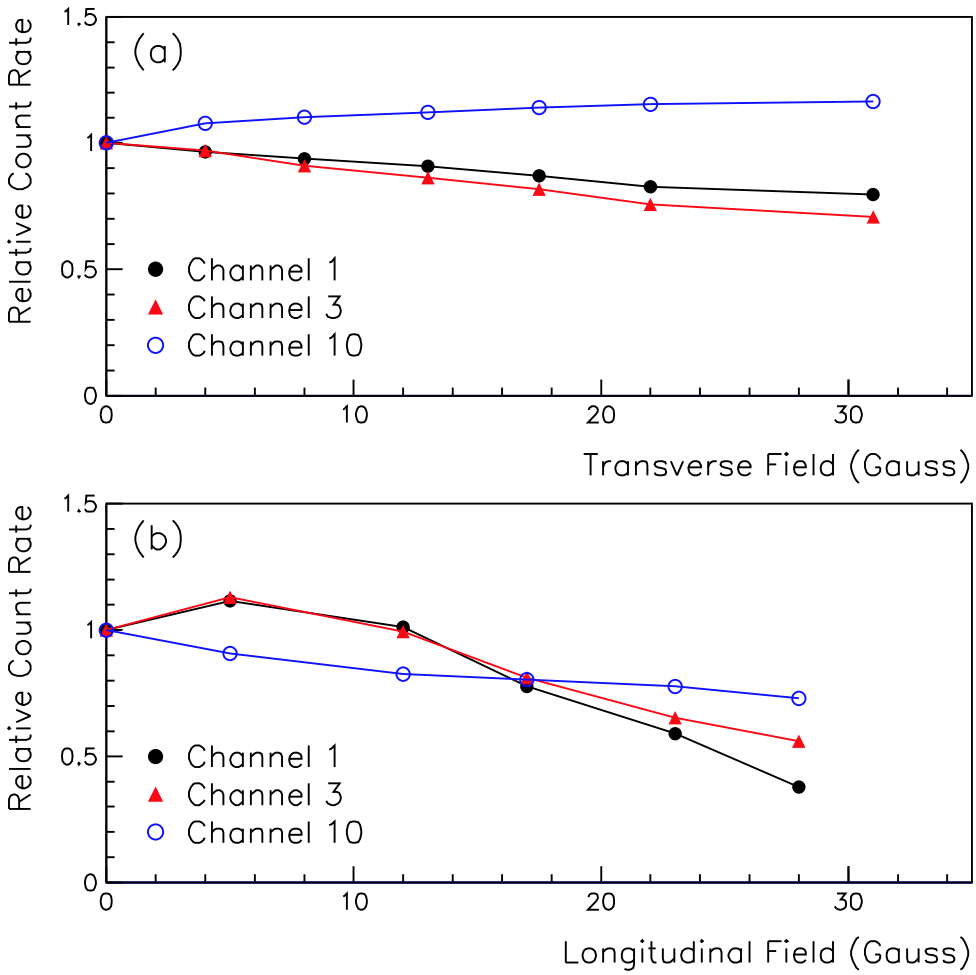

Fig. 12. Count rate as a function of the applied magnetic field without external shielding for (a)) transverse field and (b) longitudinal field.

2.5 Electronics, Trigger and Data Acquisition

The MAPMTs are plugged into a custom PCB baseboard that contains the VDN's and signal routing. Each baseboard hosts 16 MAPMTs, a total of 256 channels, and passes the signals along a 34-conductor cable to two hybrids one above and one below the support channel. Each hybrid hosts two 64-channel ASICs, thus accommodating 8 MAPMTs.

The front end electronics used in the test beam is based on custom made VA_MAPMT ASICs produced at IDE AS, Norway. [2] Multiplexer boards (MUX), designed and developed at Syracuse, provide the interface with a PCI based data acquisition system designed and produced at Fermilab [7]. A system diagram describing one of the readout chains is shown in Fig. 14.

The key elements in this data acquisition system are contained on pairs of

[2] Ideas ASA, N-1330 Fornebu, Norway; http://www.ideas.no.

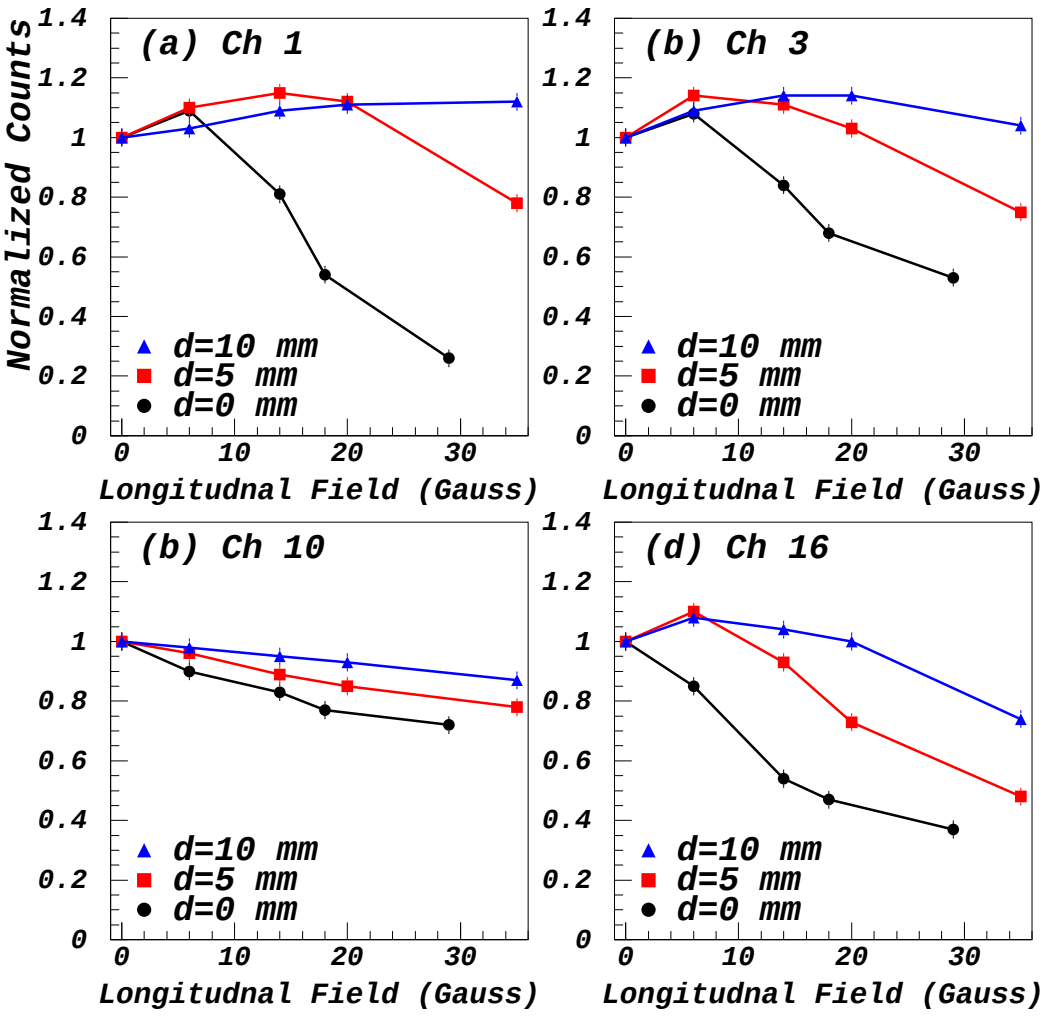

Fig. 13. Count rate as a function of the applied longitudinal magnetic field for shield extension values, d=0 mm, 5 mm, and 10 mm, for (a) Channel 1, (b) Channel 3, (c) Channel 10, and (d) Channel 16.

mating boards. The mother-board (PTA) is connected to a LINUX PC via a PCI bus. It contains the basic functionality to interface the online processor to the front end system, a sizeable memory to store the events and a variety of registers that allow the customization of the readout procedure to a variety of different systems. The mating board (PMC) contains a large FPGA (Xilinx Virtex PRO) that permits customization of the DAQ. We used the general PTA firmware developed for the BTeV pixel test beam [7], but wrote the PMC firmware suitable for our data architecture.

Two finger size scintillation counters were placed in front of the RICH tank in the horizontal and vertical directions and an additional one arranged vertically was placed behind the tank. They were aligned to beam particles. We also

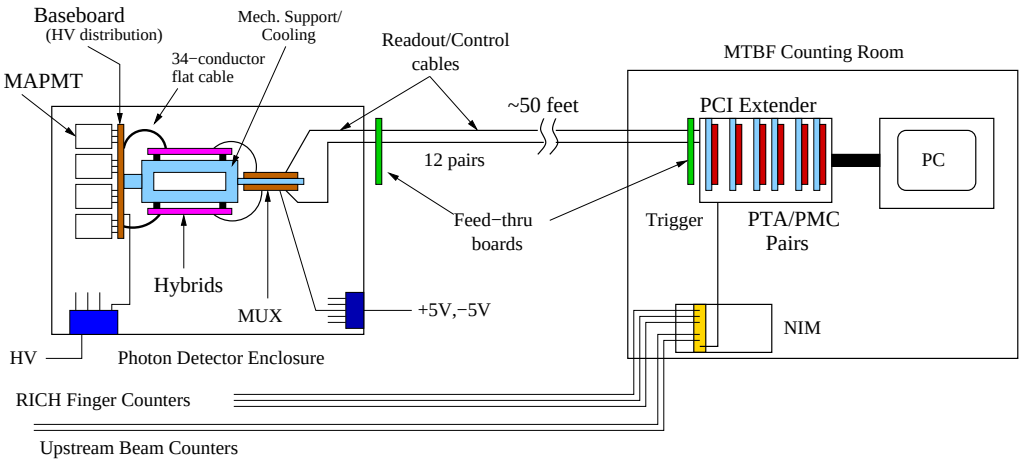

Fig. 14. Diagram showing major components of electronic read-out system.

used two larger beam defining counters upstream. Our trigger was formed as a coincidence of the beam counters and local finger counters. The trigger signal required the coincidence of all five scintillators. The typical trigger rate was 300-500 Hz, during data-taking. The beam spot at the entrance window of the RICH prototype tank was ∼5 mm in diameter. The r.m.s. angular divergence of the beam was <0.25 mrad. This trigger signal was used to move the data from the local buffers in the front end hybrids to the PTA memory.

2.5.1 Front End Electronics

The VA_MAPMT ASICs comprise 64 mixed analog and digital processors with parallel inputs and parallel outputs. The parameters affecting its mode of operation are loaded through an input shift register initialized at the beginning of a data taking cycle.

Fig. 15 shows the conceptual diagram of each readout channel. The analog section comprises a semi-gaussian preamplifier and shaper circuit, followed by a high pass filter that has the purpose of reducing the sensitivity of the discriminator to long range drifts of the DC working point of the device. In addition, a voltage-controlled pole-zero cancellation circuit is introduced to optimize the rate capabilities. The analog section is optimized for low noise performance with an expected gain of 10^6.

The input of the digital section is a discriminator that must operate effectively at very low thresholds and it needs to tolerate very high rates, of the order of several MHz, to cope with the high occupancy that was expected in some areas of the BTeV RICH. The discriminator threshold is set through an external 8 bit DAC. In addition, a 4 bit programmable DAC is built in every channel to fine tune the threshold of each individual channel to compensate for different DC

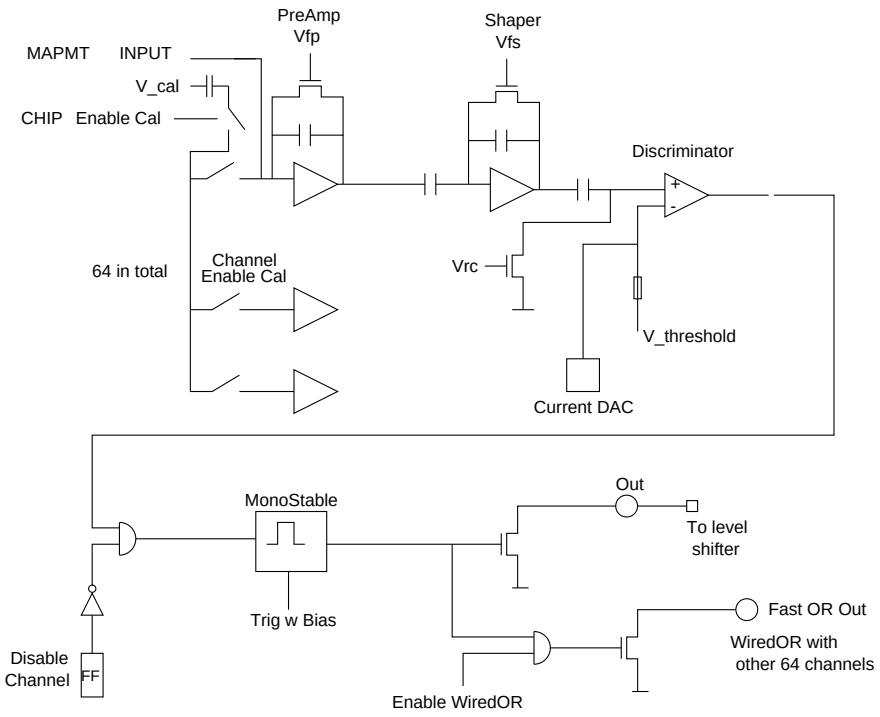

Fig. 15. Block diagram of an individual readout channel of the front end ASICs described in this paper.

offsets. The discriminator output drives a monostable circuit that produces an output current pulse whose width is about 100 ns. Individual digital outputs can be disabled through a channel mask set during the initialization sequence.

There are three modes of operation for this ASIC: (1) an initialization sequence, when a bit pattern sequence is shifted in the ASIC to program the desired operating conditions; (2) a calibration mode, when channels selected in the initialization sequence respond to an input current pulse sent to the calibration input; (3) finally, in normal mode, all the working channels are activated and respond to charge signals collected at their inputs. In addition, a fast-OR of all the channel hits can be activated for monitoring or synchronization purposes.

Fig. 16 shows the hybrid hosting the VA_MAPMT ASICs. It is a conventional 6-layer rigid printed circuit board. The 64 parallel current outputs of the VA_MAPMT ASIC are wire-bonded to the inputs of a level-shifter ASIC that produces TTL logical signals matching the input requirements of the XILINX Virtex 300 FPGA, used to drive the initialization sequence and they latch and transfer the data from the front end to the back end circuit with the protocols needed by the data acquisition system. The firmware is downloaded in the first step of the initialization sequence and thus we can adapt this hybrid to different data taking modes, and different triggering configurations.

Fig. 16. VA_MAPMT ASICs mounted on the hybrids used in the BTEV gas RICH prototype studied with test beam runs at Fermilab.

2.5.2 Data acquisition architecture

There are two firmware modules that were developed for this test beam to allow for triggered data acquisition: a hybrid firmware, implementing the ASIC initialization and the timing necessary to synchronize the data flow with the trigger signal, and a PMC firmware, to interface this data structure with the general data acquisition framework.

Two elements needed to be implemented in the hybrid firmware: a wait period to compensate for the delay between the scintillator trigger and the prompt binary information appearing a few ns after a charge signal exceeded the given threshold. The binary output was only 100 ns wide, to allow for the fast data rates expected in the real experiment, and thus it decayed before the corresponding trigger was available at the hybrid boards. Secondly, a time stamp mechanism was necessary to allow the combination of event fragments from different hybrids.

Channels registering a signal above threshold self-latched and initiated a delay signal matching the expected trigger delay. At the end of this wait period, if a trigger signal was asserted, the data were pushed out of the hybrid onto the PMC board, whereas if no trigger occurred, the latches were reset and the hybrids were ready for a new event. When a channel was latched, the corresponding 6-bit event counter information was latched in the hybrid. The event counters in the various hybrids were driven by a global synchronization clock provided by one of the PMC cards, the master card. The master card distributed the clock to the other cards which, in turn, distributed it synchronously to all the front end hybrids.

The PMC cards received the signals coming from 2 hybrids. Their main functions were the generation of an "extended time stamp," using a 26 bit counter synchronized with the local time stamp counter. Subsequently the formatted events, including the hybrid address, were sent to the online PC for further processing.

The DAQ software [8], originally developed for the BTeV pixel beam test, was implemented in C++ and encompasses three main processes: Producer, Consumer and Logger. The Producer is the component which works mostly with the PTA/PMC pair. It sends the control signals necessary to drive the data acquisition and receives data from the local memories. The Consumer process reads and analyzes the data. The Logger receives messages from the other components and notifies the user in case of errors.

2.6 Gas System

A gas system was designed and built to circulate and purify the C_4F_8O radiator gas. The design was intended to be open and passive, not requiring complicated feedback with precise pressure monitoring. As a consequence, an expansion bellows was mounted above the main RICH tank, which expanded to take up the volume of a gas charge when injected into the system, and compensated for variation in atmospheric conditions. A simplified schematic of the system is shown in Fig. 17.

There are two main circuits in the system. The first is the compression circuit, which consists of the main RICH tank, expansion bellows, high-pressure pump, small condensation tank, C_4F_8O gas bottle, and a filter pack. This is the outer circuit shown in the flow diagram. Initially the system is flushed with Argon. Filling with C_4F_8O gas is accomplished by pressure differential flow from the bottle through the filters to the main tank. The flow rate is controlled so as not to stress the acrylic windows on the main tank, and the expansion bellows expands to hold the extra gas volume. When the bellows reaches its maximum extent, the large pump is turned on, and the gas (a mixture of Argon and C_4F_8O) is compressed in the small condensation tank. When the pressure in the condensation tank reaches $\sim$25 psig, the C_4F_8O gas liquifies; and when the pressure reaches 33 psig, a relief valve opens releasing the gas (mostly Argon) until the pressure falls below the relief level. In this way, the fluid mixture is purified of Argon (as well as any residual air).

A new C_4F_8O gas charge is injected from the bottle, passing through the filter pack, and into the main tank, again filling the expansion bellows. The filter pack consists of a coalescer, a molecular sieve and a particulate filter to remove water vapor and particulates from the gas. This compression process is

repeated iteratively until the required purity is reached. After a few cycles, a valve is opened to allow the C_4F_8O liquid in the compression tank to vaporize and re-enter the circuit as a new charge. In this beam test, $(94 \pm 2)\%$ purity by weight was achieved asymptotically. This was the maximum possible in the system, limited by the existence of a small volume at the top of the condensation tank that was inaccessible to liquid. The remaining gas in the system was argon that is transparent in the wavelength range of interest.

The second circuit in the system is the circulation circuit, which consists of the main tank, expansion bellows, filters, and a small pump. It is the inner circuit shown in the flow diagram. This circuit is run when the tank is filled with sufficiently purified C_4F_8O gas, and is intended to maintain the radiator gas at a constant composition during data taking.

The circuits were controlled and monitored by the PLC-based iFix DMACS^{TM} system from General Electric-Intellution, which provided the computer interface for controlling the pumps and reading the transducers for pressure, flow, temperature and humidity. A height sensor on the expansion bellows allowed for a simple feedback loop to control the high-pressure pump. All process variables were recorded. Overall the C_4F_8O gas system worked well, as designed. We did find, however, that the expansion volume while useful for a test system would be too cumbersome to include in the final detector. Rather the actively controlled gas systems similar to those used on the DELPHI [9] or HERAb [4] RICH systems would be more appropriate.

2.7 C_4F_8O Gas Compatability

Since C_4F_8O has never before been used as a Cherenkov radiator, its chemical compatability with other materials needed to be investigated. To this end, C_4F_8O gas was tested in contact with a variety of plastics, epoxies, metals and other materials, as listed in Table 1 [10].

The C_4F_8O gas and all materials (except water) were put into the same specially-designed gas-tight stainless steel vessels and kept at an elevated temperature (80°C) and pressure (1.2 atm) for several months to accelerate the chemical kinetics of any possible reactions. This represented a worst-case test. After periods lasting up to 9.6 years exposure (20°C equivalent), the C_4F_8O gas was analyzed via Gas Chromatography and Proton NMR. No measurable amounts of reaction products were obeserved. The materials exposed were tested for relevant physical properties: change in dimensions, weight, epoxy strength, and optical transmission (e.g., UVT acrylic). No measurable material changes were detected, [3] and no optical changes were seen larger than the

[3] There was a slight effect, however, in lightening the color of the surface of the

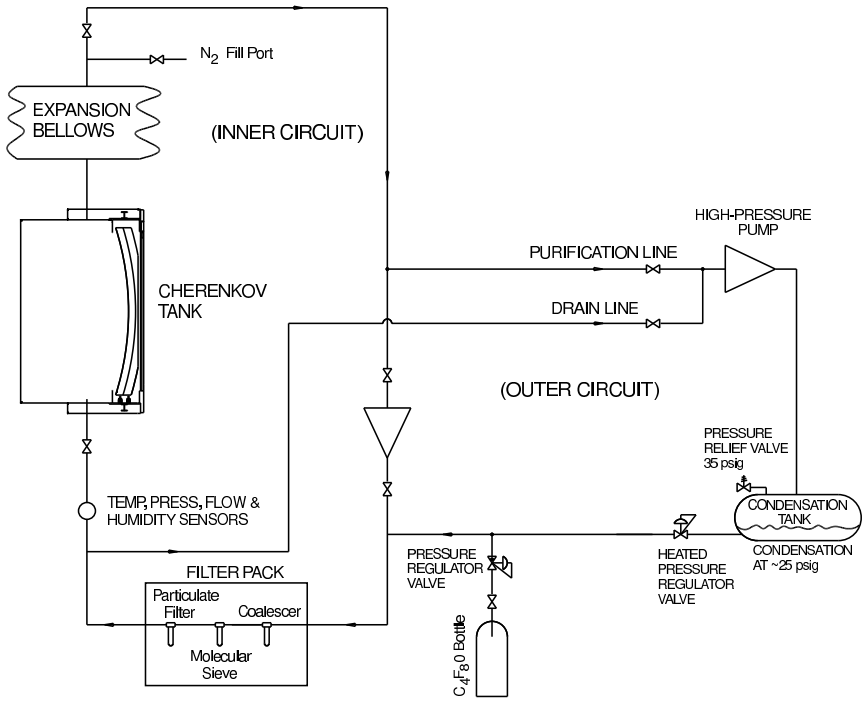

Fig. 17. Simplified flow diagram of the C_4F_8O radiator gas circulation and purification system.

sample-to-sample variation (<2% above 290 nm, <5% below).

Water is a special concern for C_4F_8O, since the Oxygen atom was thought to make it potentially reactive, forming HF. However, in a separate test with only water exposure to C_4F_8O gas for up to 13.5 years equivalent, gas chromatography analysis found the total contaminants picked up by the gas to be <50 ppm (resolution of the device), and proton NMR studies gave no indication of any H-based contaminants. There was no measurable HF production.

3 EXPECTED RESULTS

The separation between pions and kaons in Cherenkov angle is given by [11]

$$\Delta\theta = \cos^{-1}\left(\frac{1}{n(\lambda)\beta_\pi}\right) - \cos^{-1}\left(\frac{1}{n(\lambda)\beta_K}\right) \quad , \tag{1}$$

Copper tube after 4 years equivalent exposure. Electron-dispersive X-ray analysis did not indicate the presence of Fluorine on the Copper surface to a depth of 1 μm. A control vessel filled with dry N_2 exhibited a similar result. This is most simply understood as a temperature induced effect.

Table 1
Materials tested for compatability with C_4F_8O.

Class	Materials
Possible reactants	Water
Window materials	UVT Acrylic, Borosilicate Glass
Mirror materials	Continuous Fiber Reinforced Plastic (CFRP), Mirror matrix
	Beryllium metal, Beryllium with CYTEC BR-127 primer
Construction metals	Aluminium, mild Steel, Stainless Steel, Copper, Brass
Composite materials	Teflon, Kevlar, Carbon Fiber, FR-4
Epoxies	Armstrong A-12, Hysol, Araldite
O-Ring materials	Viton, Buna-N, Neoprene
Other materials	Poly-flo tubing

where $n(\lambda)$ is the wavelength dependent index of refraction and β_i is the particles momentum divided by its energy.

Thus determination of the expected separation requires knowledge of the index of refraction, properly weighted by the wavelength acceptance and the fact that Cherenkov light is generated with a $1/\lambda^2$ spectrum.

We have measured the refractive indices of C_4F_8O, C_4F_{10} and also C_4F_8 at three different wavelengths using a Michelson interferometer. The results are shown in Fig. 18. The curve is an analytical expression for the C_4F_{10} index based on extrapolating DELPHI measurements of the C_4F_{10} index in the ultraviolet region of the spectrum [12]. We use this curve to model the wavelength dependence of the index of refraction as we do not have measurements over all the detector bandwidth, which extends down to 280 nm. We are mostly insensitive to the actual value of the index, but need to model the wavelength dependence to estimate the chromatic aberration.

The ability to identify particles depends not only on their inherent separation in Cherenkov angle, but also upon the resolution provided by the system. We model the expected resolution by using a full Monte-Carlo simulation of the radiation and detection of Cherenkov photons. Photons are generated according to the known Cherenkov formula including polarization [11]. Wavelength dependence of the refractive index is taken into account. The transmission and reflection of all optical elements are taken into account using a ray tracing method. This includes the wavelength dependent transmission of the acrylic window. The quantum efficiency of the MAPMTs as a function of wavelength is shown in Fig. 19; it includes the cutoff due to the boroscilicate window. The curve is based on Hamamatsu measurements. The collection efficiency of

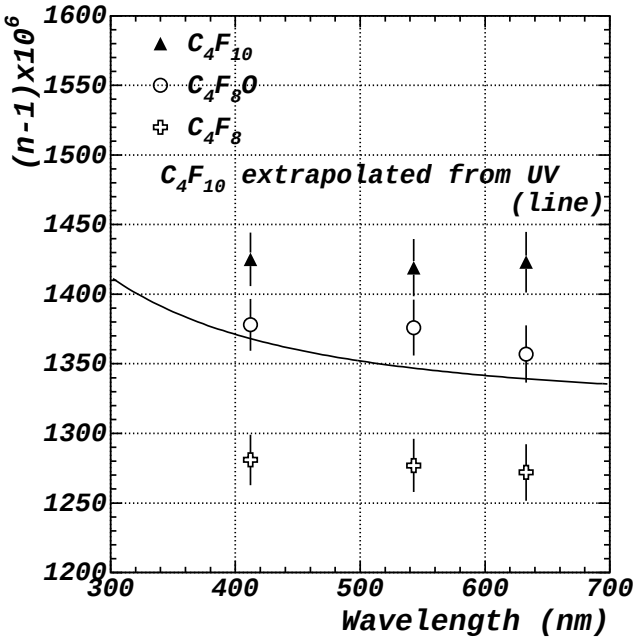

Fig. 18. Our measurement of the index of refraction of three gases corrected to 1 atmosphere pressure and 22°C nominal temperature. The curve is an extrapolation of C_4F_{10} measurements at shorter wavelengths that is used in the simulation.

electrons to the first dynode reduces the yield by an additional 77%. The gas transmission is assumed to be 100% in our wavelength region. Using these numbers as input, for a 3 meter long C_4F_8O radiator at room temperature, we expect to detect 46.3 photoelectrons for a high momentum track with an angular resolution per photon of 0.75 mr. Therefore, after averaging over all the photons, a resolution in Cherenkov angle per track of 0.103 mr is expected, giving 4.2σ separation between 70 GeV/c pions and kaons. We note that the resolution has almost equal contributions of 0.5 mr from the index of refraction variation with wavelength (chromatic abberation), the spatial error in detecting the photons and the emission point error, which exists even in this focusing system and is magnified by the fact that the mirror is tilted by 262 mr in order to focus on the MAPMT detector plane.

For our test situation the number of photons will be somewhat less because of imperfect coverage of our photon detector and also because the gas will not be totally purified. For our measured gas mixture of (94±2)% C_4F_8O and 6% Argon, and a phototube array coverage of 93.6%, we expect 40.5 detected photons each with a resolution of 0.75 mr, yielding an expected track resolution of 0.11 mr.

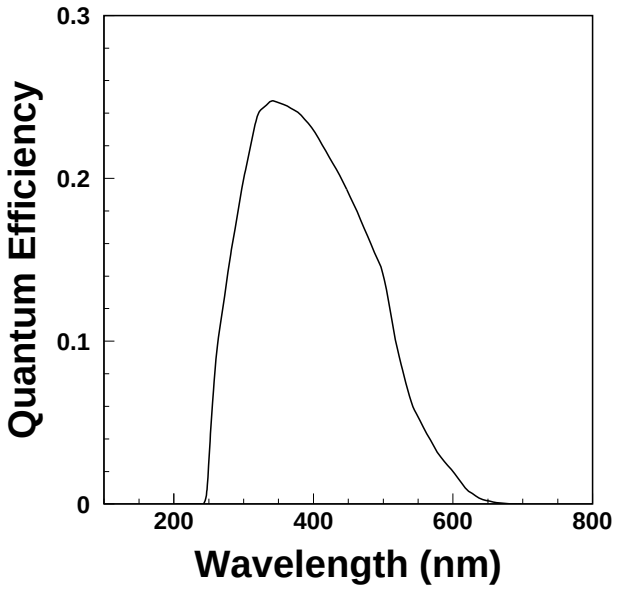

Fig. 19. The quantum efficiency versus wavelength of the MAPMT.

4 OPERATING POINT DETERMINATION: HIGH VOLTAGE AND THRESHOLD OPTIMIZATION

While in principle it should be able to operate the MAPMT system at substantial gain, we find that large pulses can saturate the electronics causing rather large voltage spikes to be reflected back on the input cables between the MAPMT and the hybrids. These sharp voltage swings then capacitively couple to neighboring lines causing extra hits in these channels, a phenomenon that we call "cross-talk." Thus determining an optimal high voltage for the system is very important. This problem is addressed in a subsequent version of the VA_MAPMT ASICs which have their dynamic ranges optimized for higher gains. For the rare remaining residual saturation occurrences, using a cable with less cross-talk would also be beneficial.

Although each of our 53 tubes has a somewhat different gain as a function of voltage, it was adequate to group them into three categories: low gain, medium gain and high gain, designated as HV1, HV2, HV3, respectively.

To investigate the performance as a function of high voltage we took data at different settings. Ring images appeared at each setting. Fig. 20 shows a typical event. With our nominal threshold setting little if no noise is evident.

The photon yield can be characterized by counting the number of hit channels. We also define a "cluster" by grouping hits together if they are in adjacent electronic channels. We are not grouping here necessarily the channels on the MAPMT surface. What we are doing is grouping the channels only by electronic address which is one dimensional rather than two dimensional. While

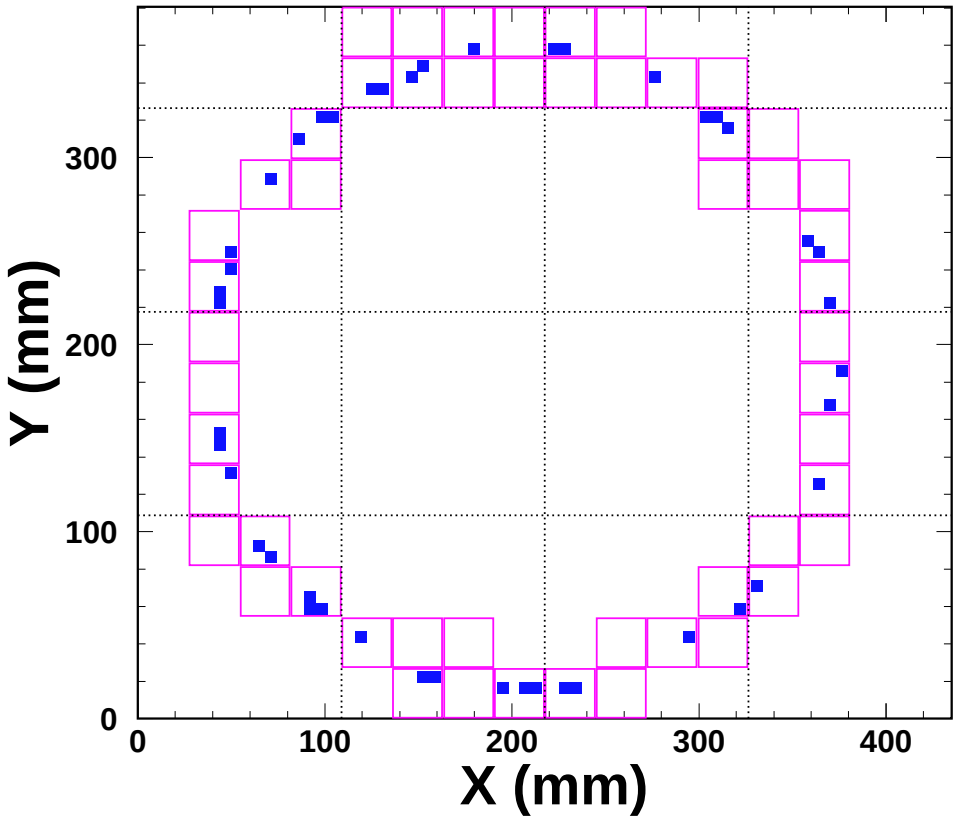

Fig. 20. One recorded ring image. Each darkened square represents a hit channel. Each solid hollowed box corresponds to a MAPMT tube.

this does inevitably group some real photons together it provides a useful way, in the presence of cross-talk, of searching for a region where our performance is independent of high voltage, usually called a plateau. We also use the average cluster size.

Fig. 21 shows the number of hits, the number of clusters and the average cluster size for each of the three groupings of tubes as a function of high voltage. We choose to use 800 V, 750 V and 700 V as nominal settings for the three groups, respectively.

A blue LED was employed to independently evaluate the size of the cross-talk induced effects. The setting was such that only zero or one photon was typically detected on any single tube in each pulse. The cluster size as a function of voltage is shown in Fig. 22. We estimate that at our nominal voltage setting only 5% of the observed photons are due to cross-talk.

The threshold setting controls the level for which signals are counted. In Fig. 23 we show the variation in the number of hits, number of clusters and cluster size as a function of threshold from beam data. (The threshold voltage is negative; more negative values result in higher thresholds.) The nominal threshold is -7.85 mV which corresponds to 49,100 electrons. This threshold is at least ten

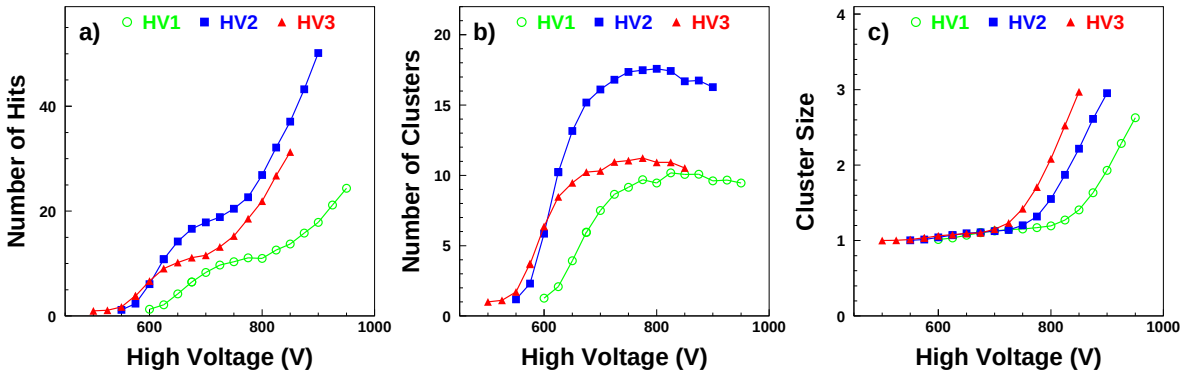

Fig. 21. a) The number of hits, b) the number of clusters and c) the average cluster size for each of the three groupings of MAPMT tubes as a function of high voltage.

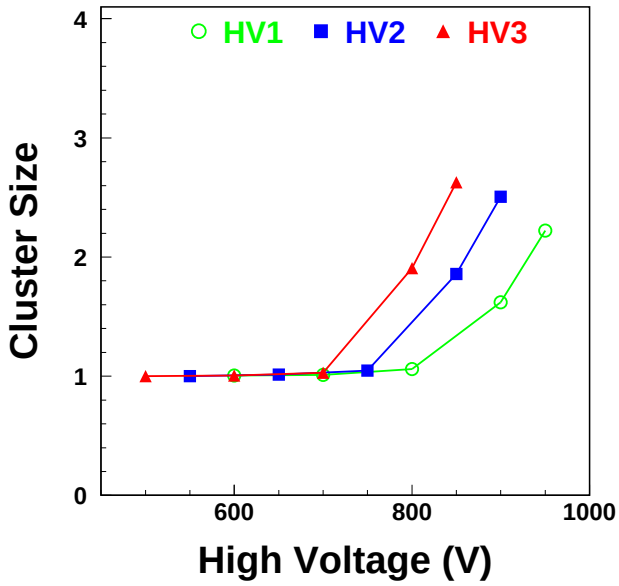

Fig. 22. The average cluster size for each of the three groupings of MAPMT tubes as a function of high voltage, using the LED pulser instead of the proton beam.

times smaller than the mean charge expected from a single photon. We tried to use a lower threshold, but did not see any efficiency improvement. Our results are not very sensitive to threshold which is kept as it was for the previously mentioned studies (-7.85 mV) unless specifically indicated.

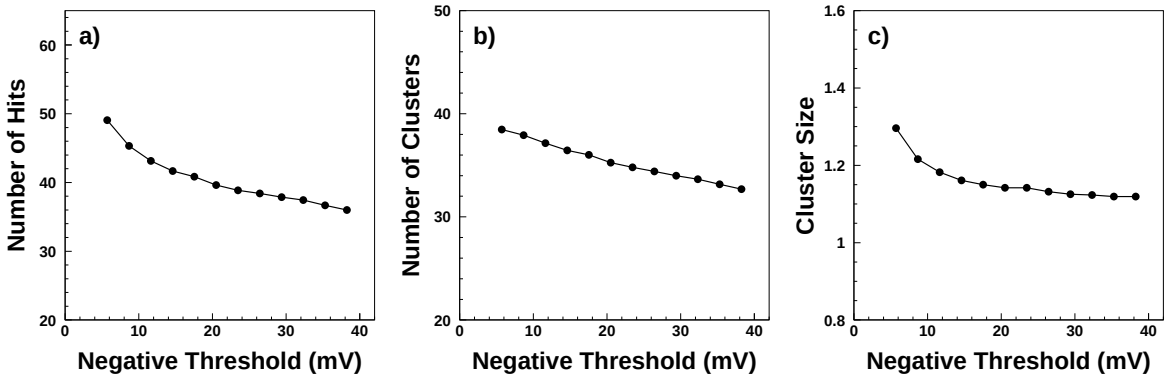

Fig. 23. a) The number of hits, b) the number of clusters and c) the average cluster size as a function of threshold in mV. The lowest threshold of 4.2 mV corresponds to about 26,200 electrons.

5 RESULTS

5.1 Refractive Index

We determine the effective refractive index from a fit to the diameter of the Cherenkov rings, after correction to nominal pressure (1 atm) and temperature (22°C). After correcting for the (6±2)% of Argon, we find that the index of refraction for C_4F_8O is 1.001389±0.000024 for the wavelength interval of 280 - 600 nm weighted by the $1/\lambda^2$ input Cherenkov light distribution, the window transparencies and the MAPMT efficiencies. The error is dominated by the uncertainty in the gas purity. The value obtained here is consistent with the measurements obtained using the Michelson interferometer (see Fig. 18).

5.2 Photon Yield and Cherenkov Angular Resolutions

We count photons about the mean Cherenkov angle for photons generated by the track, each within three standard deviations of the single photon resolution. The photon yield for an ensemble of tracks is shown in Fig. 24. The large shaded peak corresponds to single tracks with a mean value of 43.1 photons, having a Gaussian r.m.s. of 6.5 photons. The second peak is due to two tracks arriving close in time. Although we predict 86.2 photons in this peak, a Monte Carlo simulation taking into account that the tracks are very closely correlated in both space and angle shows that we expect only 76.9 photons, due to overlapping photons, consistent with our observations. There is also a small tail toward low hit numbers due to bad triggers or event fragments.

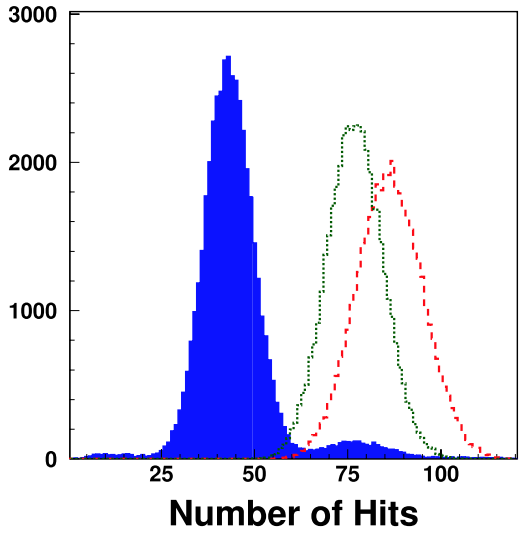

Fig. 24. The photon yield per track at nominal high voltage and threshold settings (solid). The dashed curve shows the Monte Carlo expectation for two tracks without considering overlap of photons, while the dotted curve explicitly takes into account the overlap possibility.

The measured yield of 43.1 photons is larger than the Monte Carlo expectation is 40.5 photons. The 6.5% excess we observe is consistent with the expected cross-talk, but may also be due to a somewhat higher MAPMT quantum efficiency than expected.

The angular resolution per photon is shown in Fig. 25 (a). It is determined by plotting the measured Cherenkov angle for each photon minus the expected Cherenkov angle, determined by knowledge of the incident track angle. We measure an angular resolution per photon of 0.79 mr while the Monte Carlo expectation, shown in (b) is 0.75 mr. [13]. The difference is consistent with being due to the $\sim$5% cross-talk.

The Cherenkov angle per track is determined by averaging all detected photons within three standard deviations of the single photon resolution. In Fig. 26 we show the measured Cherenkov angle for each track minus the expected Cherenkov angle. The angular resolution per track is 0.1164 ± 0.0004 mr as determined by a fit to a single Gaussian. It is slightly poorer than the Monte Carlo expectation of 0.112 mr.

We now examine the track resolution as a function of high voltage. Fig. 27 shows the number of hits, the Cherenkov angular resolution per photon and the Cherenkov angular resolution per track as a function of HV2, the high voltage applied to group 2. All groups are included here, however with HV1 being 50 V higher and HV3 50 V lower.

Viewed in terms of the angular resolution per track the voltage plateau extends over a range of 100 V. Any higher or lower voltage results in a poorer

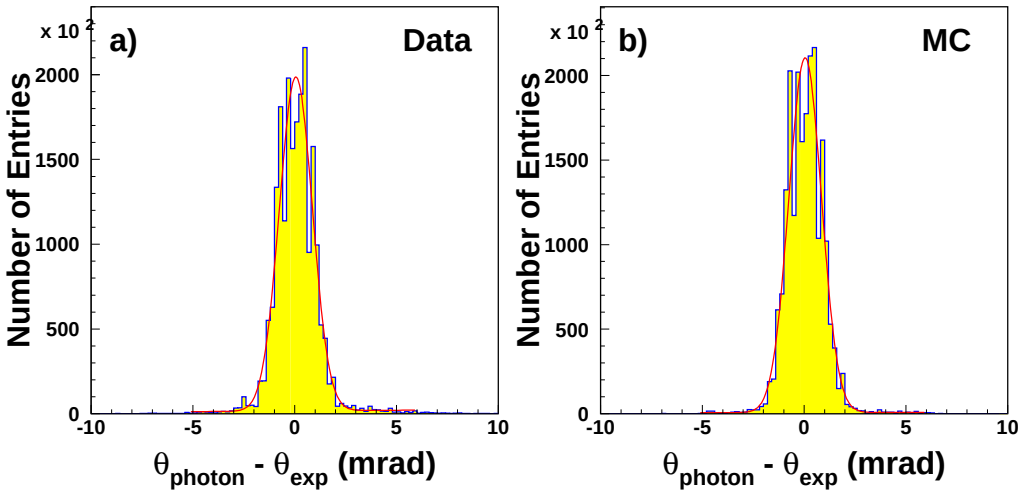

Fig. 25. The difference between measured and expected Cherenkov angles for single photons in a) data and b) MC at nominal settings.

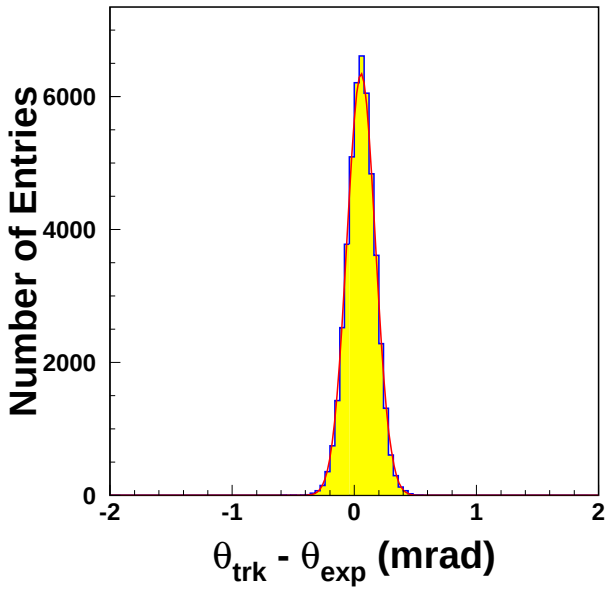

Fig. 26. The measured Cherenkov angle minus the expected Cherenkov angle for each track.

resolution. At the higher voltage this is due to cross-talk and at the lower voltage a loss of hit efficiency. The high voltage plateau can be extended by using the next generation of front end ASICs and/or with better signal cables.

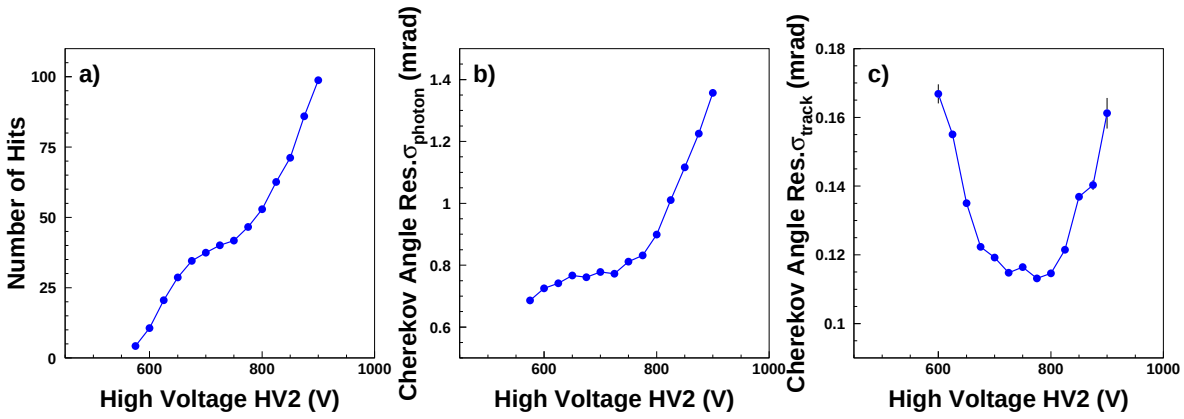

Fig. 27. a) The number of hits, b) per photon Cherenkov angle resolution, and c) per track Cherenkov angle resolution as a function of high voltage. Data are from all three groups of MAPMT tubes. HV for the other two groups (HV1, HV3) are set to be 50 V higher and 50 V lower respectively.

6 CONCLUSIONS

We have constructed a focussed ring imaging Cherenkov detector and exposed it to a 120 GeV/c proton beam at Fermilab. Using a 3 meters length of C_4F_8O gas radiator and R8900-M16 multianode photomultiplier tubes we measure about 43.1 photons per track with an angular resolution of 0.79 mr per photon and a track resolution of 0.116 mr. We expect that 5% of the photons were generated by cross-talk largely due to a mismatch between the dynamic range of the front-end electronics and the gain of the MAPMTs. The gas contained 6% Argon and the photon detector covered 93.6% of a circle. In a final system the Argon would be eliminated and the phototube coverage would be complete.

Based on these measurements, if we used pure gas and had complete photon coverage, we would expect to have 46.6 photons and an angular resolution per track of 0.109 mr. Our simulation using these parameters gives the same number of photons and a slightly better track resolution of 0.103 mr, since the simulation here doesn't include the cross-talk. This system would be an excellent identifier of particles.

Sometimes the parameter $N_0 = N_\gamma / L \sin^2\theta$, where N_γ is the number of detected photons, L the detector length and θ the Cherenkov angle is used to characterize RICH systems [14]. This system would have an N_0 of 58/cm. The usefulness of a RICH system, however, is given by its ability to separate particles. N_0 is only part of the system design. It can be increased, for example, by using photons at shorter wavelengths but the chromatic abberations associated with such a change would make the particle separation properties of the system worse, rather than better. At 70 GeV/c incident particle momentum

the angular separation between pions and kaons in C_4F_8O is 0.421 mr. This system would provide a separation corresponding to 4σ separation.

The R8900-M16 MAPMT from Hamamatsu has been shown to be an excellent photon detector, especially when coupled to low noise electronics. Bench tests confirm that the MAPMT has an active area of about 80% and the response over this area is quite uniform. For the four central channels about 20% of the photons are detected in one of the adjacent channel. The edge and corner channels have approximately a 15%, and 10% out-of-channel detection rate, respectively. This results in an acceptably small degradation in the positional resolution of the device. Lastly, we have found that these tubes can be adequately shielded for operation in environments which have magnetic fields. Shielding against the longitudinal component requires extending the tube beyond the face of the MAPMT. As long as photons are not incident at large angles, the loss due to shadowing is generally small (it was found to be at the level of 5% for the BTeV RICH).

Lastly we found that C_4F_8O is an excellent gas for Cherenkov detectors with a relatively large refractive index, and appears to be compatible with most materials.

ACKNOWLEDGEMENTS

We thank the U. S. National Science Foundation without whose support this work would not have been possible. We also thank the Dr. E. Ramberg and the Fermilab Beams Division for providing the test beam, H. Cease of Fermilab for critical engineering support, L. Uplegger for help with the data acquisition system and Terry Tope for help with gas system programming. We thank Andre Braem for measuring the mirror reflectivity.

References

[1] See "Experimental Techniques of Cherenkov Light Imaging," ed. by T. Ekelof, L. K. Resvanis and J. Seguinot, Nucl. Instr. Meth. A502 (2003).

[2] S. Blusk, Nucl. Instrum. & Meth. **A502**, (2003) 57; M. Artuso, Nucl. Instrum. & Meth. **A553**, (2005) 130.

[3] The mirror reflectivity was measured in the center of the mirror. We thank Andre Braem for making these measurements.

[4] I. Arino, *et al* (HERA-B), Nucl. Instrum. & Meth. **A516**, (2004) 445, and references contained therein.

[5] M. Artuso *et al*, Nucl. Instrum. & Meth. **A554**, (2005) 147.

[6] C.N. Brown and T.R. Kobilarcik, A New MTest Beamline for the 1999 Fixed Target Run, Fermilab Technical Memo FERMILAB-TM-2108, 2000. More details on the Facility are available at: http://www-ppd.fnal.gov/MTBF-w/.

[7] L. Uplegger *et al.*, submitted to IEEE Nucl. Sci., Nov. 2004.

[8] G. Alimonti *et al*, Nucl. Sci. Symp. Conf. Rec, 2003 IEEE Vol. 3 (2003) 1677.

[9] E. Albrecht *et al* (DELPHI), Nucl. Instrum. & Meth. **A433**, (1999) 47.

[10] R. Nandakumar, Material Compatibility Tests on C_4F_8O, BTeV Internal Document 3772-v2, 2004.

[11] J. V. Jelly, "Cerenkov Radiation and Its Applications," Pergamon, London (1958).

[12] HERA-B gives the index of refraction as a function of photon energy as

$$n - 1 = 0.0013178 + 1.723 \times 10^{-7} E_\gamma + 5.495 \times 10^{-6} E_\gamma^2 \quad . \tag{2}$$

See A. Bulla, "Die Entwicklung eines ringabbildenden Cherekov-Zählers für den Detektor HERA-B," Ph.D. thesis (1997). This formula is an extrapolation of measurements made at DELPHI in the ultraviolet wavelength region. See E. Foktitis *et al* Nucl. Phys. Proc. Suppl. **B44** (1995) 246; E. Foktitis *et al* Nucl. Instru. & Meth. **A371** (1996) 255.

[13] The statisical errors are very small ± 0.0004 mr on the measured or simulated angles due to the large statistics.

[14] J. Séguinot and T. Ypsilantis, Nuclear Instrum. & Methods, **142** (1977) 377.